THE JOURNAL OF PHYSICAL CHEMISTRY C
A JOURNAL OF THE AMERICAN CHEMICAL SOCIETY

pubs.acs.org/JPCC Article

Different Water Networks Confined in Unidirectional Hydrophilic Nanopores and Transitions with Temperature

Frederico G. Alabarse,* Benoît Baptiste, Mónica Jiménez-Ruiz, Benoit Coasne, Julien Haines, Jean-Blaise Brubach, Pascale Roy, Henry E. Fischer, Stefan Klotz, and Livia E. Bove*

Cite This: https://doi.org/10.1021/acs.jpcc.1c01254 Read Online

ACCESS | Metrics & More | Article Recommendations | Supporting Information

ABSTRACT: The structure and vibrational properties of water molecules confined in unidirectional hydrophilic nanopores of $AlPO_4$-54·xH_2O were investigated from room temperature down to 10 K by single-crystal synchrotron X-ray diffraction, neutron pair-distribution function analysis, incoherent inelastic neutron scattering, far- and mid-infrared spectroscopy, ab initio molecular dynamics, and grand canonical Monte Carlo simulations. The ensemble of results indicates that water confined in $AlPO_4$-54·xH_2O nanopores does not crystallize down to 10 K and points at the existence of two different types of water networks, whose local arrangement and dynamical behavior become more and more distinguished when lowering the temperature below 150 K. Upon cooling, water close to the zeolite pore wall shows a highly ordered local arrangement induced by the pore wall, with a more defined site occupancy and lower density with respect to bulk water. Conversely, water in the pore core shows a denser, more disordered, and orientationally distorted arrangement and a glassy like behavior down to the lowest investigated temperature.

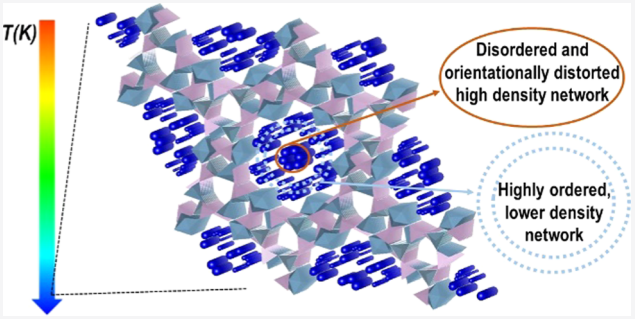

1. INTRODUCTION

The ordering of small molecules inserted in nanoporous channel systems is of great interest for applications such as molecular sieves, phase separation and heterogeneous catalysts,[1] nanotribology,[2] fabrication of nanomaterials using H_2O as a template,[3] or even for the durability of concrete.[4] As water is normally present in most molecular sieves, its order and reactivity as a function of temperature are clearly of particular importance in chemistry, geology, biology, and physics. Whatever the nature of the surface of the porous matrix (hydrophilic or hydrophobic), the restriction of the accessible space induced by nanoconfinement has important structural, dynamical, and thermodynamic consequences.[5] Over the past two decades, a series of studies have been done on water confined in different nanoscopic porous materials,[6−11] both crystalline and amorphous, and have indicated the universal lowering of the water freezing point, while no general agreement has been reached on the conditions of suppression of crystallization by confinement, in terms of pore size, pore structure, and nature of the water−surface interaction. As an example, Mo-based capsules, which contain a large number of pores, are used as nanocontainers/nanosponges to study water confined in strong confinements.[12] The authors have shown that, by changing the chemical composition of the internal cluster shell, it was possible to influence the structures of encapsulated nanodrops of water. A very recent example concerns the reported ordering of the water wetting-layer in single-walled aluminogermanate imogolite nanotubes.[13] Water confined in a bioactive glass with 5.9 nm pore diameter was also the subject of recent temperature-dependent structural studies: results have pointed at a nonhomogeneous ordering of water molecules inside the pores, whose local organization depends on the distance from the pore surface.[14]

Some studies have shown that, for temperatures below the bulk water freezing point, water confined in hydrophobic nanopores crystallizes.[6−9] Such a phenomenon is also supported by studies showing the formation of ice nanotubes in carbon nanotubes.[8,9] A different scenario was reported concerning the freezing of water in hydrophilic nanopores down to 173 K. The pore surface can induce orientational order of water in contact with its wall (proximal water), while water in the pore center (inner water) is more disordered.[15] Crystallization of proximal water is believed to be suppressed as the number of hydrogen bonds (HBs) formed is insufficient, while crystallization of the inner water could be hindered as the curvature prevents the formation of a network of tetrahedrally coordinated molecules. However, this point needs to be proven

Received: February 10, 2021
Revised: June 14, 2021

by a systematic study at $AlPO_4$-54·xH_2O confined water at lower temperatures.

Water confined in the nanopores of hydrophilic $AlPO_4$-54·xH_2O has been the subject of several recent studies involving variable pressure−temperature conditions.[15−22] $AlPO_4$-54·xH_2O (hexagonal VFI structure, space group $P6_3$, a = 18.9678(13) Å and c = 8.0997(4) Å, $Al_{18}P_{18}O_{72}$·xH_2O)[18] exhibits highly hydrophilic one-dimensional (1D) pores along the **c** direction, with a diameter of 12.7 Å, which are among the largest pores known for zeolites and aluminophosphates. In the pores, H_2O molecules form a disordered hydrogen-bonded network at ambient temperature and pressure. $AlPO_4$-54·xH_2O represents an interesting target material to study nanoconfined water under strong confinements. The zeolite framework is built up of 4-, 6-, and 18-membered rings of alternating AlO_6, AlO_4, and PO_4 polyhedra. One-third of the aluminum cations are octahedrally coordinated due to the presence of two H_2O molecules in their coordination sphere. Synchrotron single-crystal structural studies at ambient conditions reported the presence of 36 water molecules in its pores, with 11 further H_2O molecules identified by molecular dynamics simulations, as these molecules were too mobile to be detected by single-crystal X-ray diffraction (XRD).[18]

From a dynamical point of view, superdiffusion effects have been predicted to occur for water nanoconfined in the unidimensional pores.[17] Upon lowering the temperature at ambient pressure, full ordering of nanoconfined water was not observed down to 173 K,[15] but water ordering and site occupancies of proximal water were shown to increase as the temperature decreases, likely because water molecules interact with the nanopore wall forming HB with O atoms of the framework.

Here, we report a series of new experiments probing both structural and vibrational properties of H_2O in $AlPO_4$-54·xH_2O hydrophilic nanopores down to 10 K by single-crystal synchrotron X-ray and powder neutron diffraction measurements, incoherent inelastic neutron scattering (INS), far- and mid-infrared spectroscopy, ab initio molecular dynamics (AIMD), and grand canonical Monte Carlo (GCMC) simulations. These new results clearly indicate that water in the zeolite nanopores does not crystallize even at the lowest investigated temperature and reveals an increasingly different structural and dynamical behavior of proximal and inner water on cooling: while proximal water shows an increase in the orientational order, as well as an increasing localization of molecules at the pore sites and a strengthening of the water−water interactions, inner water exhibits increasing disorder and an amorphous glasslike behavior.

2. METHODS

The ordering of water confined in the $AlPO_4$-54·xH_2O nanopores was investigated using two samples: small polycrystals and large single crystals. The small polycrystals (linear dimensions on the order of 30 × 1 × 1 μm^3) were synthesized from nanometric alumina (Pural SB) and phosphoric acid by an optimized sol−gel procedure followed by hydrothermal treatment as described previously.[15,16] The high-quality single crystals (needlelike 200 × 25 × 25 μm^3) were synthesized from an alternative method using polyphosphoric acid; details can be found elsewhere.[15] The dehydrated phase ($AlPO_4$-54) was obtained by keeping the sample at 293 K and 10^{-6} mbar overnight. This room-temperature treatment removes the pore water while retaining a small amount of the water coordinated at the 6-fold Al.[20,21]

The dehydration of $AlPO_4$-54·xH_2O was recently studied in situ as a function of vacuum pressure at room T.[20] While nonvacuum-dried $AlPO_4$-54·xH_2O contains close to 24 wt % H_2O[22] corresponding to an x value of about 2.14, when the material is exposed to primary vacuum (5 Pa), pore water is rapidly removed and x drops to 0.25 and further to x = 0.12 when exposed to secondary vacuum (0.05 Pa).[20] The residual amount of water has been identified with the one trapped in the Al polyhedra. As a comparison, if only structural water remains in $AlPO_4$-54·xH_2O, then x would be 0.67.

X-ray diffraction (XRD) measurements on an $AlPO_4$-54·xH_2O single crystal were performed at 50, 100, and 135 K. The 50 K measurement (λ = 0.6717 Å) was carried out on the 4-circle diffractometer on the CRISTAL beamline (SOLEIL Synchrotron/Gif-sur-Yvette) using a Cryo Industries of America He gas stream cooler. A thin needle-shaped crystal was selected in oil and mounted within a cryoloop. The intensities were collected from a phi scan with a two-dimensional (2D) CCD detector placed at 80 mm from the sample using a 200 × 200 μm^2 beam size. The measurement at 100 K was realized at the XRD platform of the Institut Parisien de Chimie Moleculaire (IPCM, Sorbonne Université) on a 4-circle Bruker AXS Kappa-APEX II diffractometer (Mo Kα, λ = 0.71073 Å) using an Oxford Cryosystem N_2 cryostream. The data at 135 K were collected at the Institute Charles Gerhardt Montpellier on a Bruker D8 Venture 4-circle diffractometer equipped with an Incoatec Mo Kα microsource and a Photon II detector and combined with an Oxford Cryosystem N_2 cryostream. In all cases, data reduction, cell refinement, space group determination, scaling, and empirical or analytical absorption correction[23] were performed using CrysAlisPro software[24] or Bruker APEX3 software. The structures were solved in the hexagonal $P6_3$ space group through the Olex2[25] program by direct methods using SHELXS.[26] The refinement was then carried out with SHELXL[27] by full-matrix least-squares minimization and difference Fourier methods. All non-hydrogen atoms were refined with anisotropic displacement parameters. A merohedral twinning was detected, and the refinement was then significantly improved considering the (0 1 0, 1 0 0, 0 0 $\bar{1}$) twinning matrix. The R_1 factor (see Table S1 in the Supporting Information, SI-Section S2) decreased from 13.90 to 3.39% and from 14.2 to 4.11% for the data collected at 100 and 50 K, respectively. An R_1 factor of 3.31% was obtained for the data at 135 K.

Neutron scattering data for pair-distribution function (PDF) analysis were collected in the range of T = 10−300 K from 332 mg of $AlPO_4$-54·xH_2O powder loaded into a cylindrical vanadium can (5 × 20 mm sample diameter and height, respectively) on the D4 instrument (Institut Laue-Langevin/Grenoble). PDF(r) gives the probability of finding an atom at a distance r from an average atom taken as the origin; its detailed definition and calculation formalities have been described elsewhere.[28,29] D4 is a two-axis diffractometer, equipped with nine 1D position-sensitive microstrip detectors pressurized with ^{3}He gas to 15 bar for efficient detection. The diffraction patterns were measured over a large Q-range (Q_{range} = 0.5−23.5 $Å^{-1}$) using a Cu220 monochromator selecting 0.5 Å wavelength incoming neutrons, 2 × 2 horizontal slits, vertical diaphragm at 30 cm upstream from the sample, and additional vertical slits at 5 cm upstream of the sample as collimations. More information concerning the D4 instrument can be found

https://doi.org/10.1021/acs.jpcc.1c01254
J. Phys. Chem. C XXXX, XXX, XXX−XXX

elsewhere.[30] Experiments were carried out on dehydrated and hydrogenated samples at four temperature points (T = 10, 100, 173, and 300 K) at ambient pressure. The scattering data were collected over 1.5 h for T = 100, 173, and 300 K and over 13.5 h for T = 10 K.

Inelastic neutron scattering (INS) measurements of the generalized density of states (GDOS) of water confined at $AlPO_4$-54·xH_2O were performed using the IN1-LAGRANGE spectrometer (ILL/Grenoble) in a fixed-monitor regime with the 2D-focusing Cu220 monochromator. INS is an excellent technique to study water hydrogen bonding in confined media, and it has already been used in previous studies to provide information on librational modes in hydrated minerals.[31−33] The vibrational spectrometer LAGRANGE provides the high energy transfer needed to study the inter- and intramolecular vibrations of water. The scattering intensities from both the hydrated and dehydrated samples were collected at T = 10, 173, 235, and 293 K, using a Displex closed-cycle refrigerator. Then, 242 mg of $AlPO_4$-54·xH_2O powder was loaded into an aluminum sachet to give the sample thickness of ∼2 mm for the low-temperature measurements. The data were collected over the range of 26−500 meV (172−4000 cm^{-1}). The most interesting results are those below 200 meV (1600 cm^{-1}), in the region of the water librational band. The spectra were accumulated over 6 h for each temperature. More information concerning the IN1-LAGRANGE instrument can be found elsewhere.[34,35]

Mid- and far-infrared (IR) spectra of $AlPO_4$-54·xH_2O at low temperatures in the T = 17−300 K range were collected at the Advanced Infrared Line Exploited for Spectroscopy beamline (AILES, Synchrotron SOLEIL/Gif-sur-Yvette), which is equipped with a Bruker instrument IFS 125 FT-IR spectrometer modified to operate with the synchrotron source.[36] Mid-IR spectra (600−4000 cm^{-1}) were obtained with an MCT/InSb (600−5000 cm^{-1}) detector and a KBr beamsplitter. The far-IR domain was investigated using a 6 μm Mylar beamsplitter and a 4.2 K Si-bolometer detector (10−700 cm^{-1}). The spectra were acquired with a resolution of 2 cm^{-1} with 300 scans in both far- and mid-IR. The AILES beamline is equipped with a helium closed-circuit cryostat (pulse tube refrigerator cold head model CryoMec PT405) placed in a vacuum chamber setup pumped down to ∼10^{-6} mbar. The cryostat allows reaching low temperatures in the T = 4−360 K range; the sample temperature was measured with an accuracy of about ±0.1 K.[37] Measurements were acquired from low to high T. All mid- and far-IR measurements were performed in the transmission mode, the sample being placed in a sealed cell with windows of CaF_2 and polyethylene (PE), respectively, for the mid- and far-IR ranges. To avoid band saturation into the spectra, the sample powder was dispersed at 1% concentration in CdTe and at 10% concentration in polyethylene (PE), respectively, for the mid- and far-IR measurements.

Grand canonical Monte Carlo (GCMC) simulations were carried out to probe water adsorption at T = 10, 110, 173, 235, and 293 K in $AlPO_4$-54·xH_2O. Such a technique is a statistical mechanics method that simulates a system with constant volume V (the pore with the adsorbed phase) in equilibrium with a fictive reservoir of water molecules imposing its chemical potential μ and temperature T. The pressure is obtained from the chemical potential μ according to the bulk equation of state for an ideal gas. Considering that the temperatures treated here are well below the bulk critical point of water, the use of the ideal gas equation of state corresponds to a very good approximation. Indeed, for temperatures much below the critical point, the saturating vapor pressure and, hence, the density are low enough to treat the vapor phase as an ideal gas. Periodic boundary conditions are used along the three directions x, y, z to avoid finite size effects. The use of the grand canonical ensemble allows the density for confined and bulk water to be reached as the chemical potential and temperature are imposed. The water/water and water/framework ($AlPO_4$) interactions were modeled with the same interaction potentials as those used in our previous work.[15] In particular, as described in ref 15, some water molecules in $AlPO_4$-54·xH_2O (labeled in this study OW1 and OW2) have low atomic displacement parameters (ADPs), suggesting that they are nearly immobile. This result is in agreement with ab initio calculations in which a few water molecules were found to be framework molecules connected to the $AlPO_4$ framework by a short Al−O bond.[38] In the present work, the center of mass values of OW1 and OW2 were treated as fixed. For each system, the $AlPO_4$-54·xH_2O structure was allowed to relax using a force field developed for such materials while imposing the experimental cell parameters.

Ab initio molecular dynamics (AIMD) simulations were performed, and the vibrational spectra were extracted from MD trajectories, via the time Fourier transform of the velocity−velocity autocorrelation function (VACF) using the MD trajectories for each atom of the system. The AIMD simulations were performed using the CASTEP code (http://accelrys.com/products/datasheets/castep.pdf). Lattice parameters were fixed in the calculation to the values derived at T = 173, 235, and 293 K from a previous study.[15] All calculations use optimized ultrasoft pseudopotentials generated with the Perdew−Burke−Ernzerhof (PBE)[39] functional within the generalized-gradient approximation (GGA). We used a plane-wave cutoff energy of 500 eV. Optimized structures were used as input for the production of AIMD trajectories. They were first thermal-equilibrated at 300 K in the NVT ensemble over 4 ps with a 1.0 fs time step. The equilibration run was followed by a production run of 10 ps, performed also in the NVT ensemble at T = 173, 235, and 293 K. The density of states (DOS) was then computed as time Fourier transform of the velocity autocorrelation function (VACF) computed from the coordinates of each step of the trajectories, as implemented in the nMOLDYN program.[40] Details on ab initio molecular dynamics (AIMD) simulations are described in the Supporting Information (SI, Section S1).

3. RESULTS AND DISCUSSION

3.1. Single-Crystal Synchrotron X-ray Diffraction (SC-XRD). The structure of $AlPO_4$-54·xH_2O was refined at T = 135, 100, and 50 K using the structural model obtained by previous XRD measurements at 173 K (space group $P6_3$).[15] As in the previous study, introduction of twinning on the (100) face in the refinement reduced the R factor. The final R factors (see def. in Section S2 in the SI) and structural data (fractional atomic coordinates, atomic displacement parameters (ADPs; see def. in Section S2 in the SI), bond lengths, and angles) are given in Tables S1−S5 in the Supporting Information (SI, Section S2).

For all of the temperatures used in this study, a few water molecules (labeled OW1 and OW2; see Figure S1 in the SI) have low ADPs, similar to that of $AlPO_4$ framework atoms, as they are coordinated to ^{VI}Al (Table S2).[15,18] As already observed at higher temperatures, these molecules are in such a

https://doi.org/10.1021/acs.jpcc.1c01254
J. Phys. Chem. C XXXX, XXX, XXX−XXX

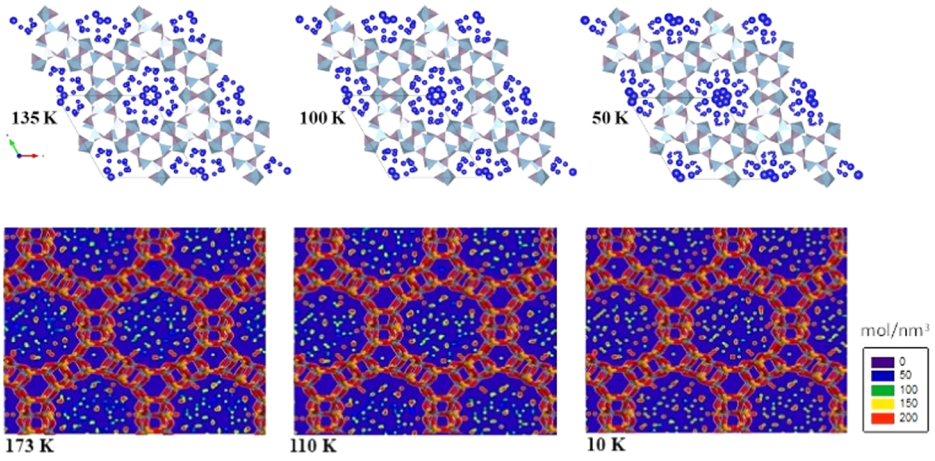

Figure 1. Experimental structure (top) and unit cell (outlined in black) of $AlPO_4$-54·xH_2O at T = 135, 100, and 50 K, obtained from single-crystal XRD. In the experimental data, the light-blue and purple polyhedra are the AlO_4, AlO_6, and PO_4 units of $AlPO_4$, while the dark-blue circles indicate the O atoms of water molecules (the O ADP are represented at 50% probability). Simulated structures (bottom) of water in $AlPO_4$-54·xH_2O at T = 173, 110, and 10 K. These simulated data are density maps of water in $AlPO_4$-54·xH_2O. The density scale increases linearly from purple, blue, green, yellow, orange, and red. Note the higher ADP and lower density from inner water compared to proximal water for all studied T in both experiments and simulations.

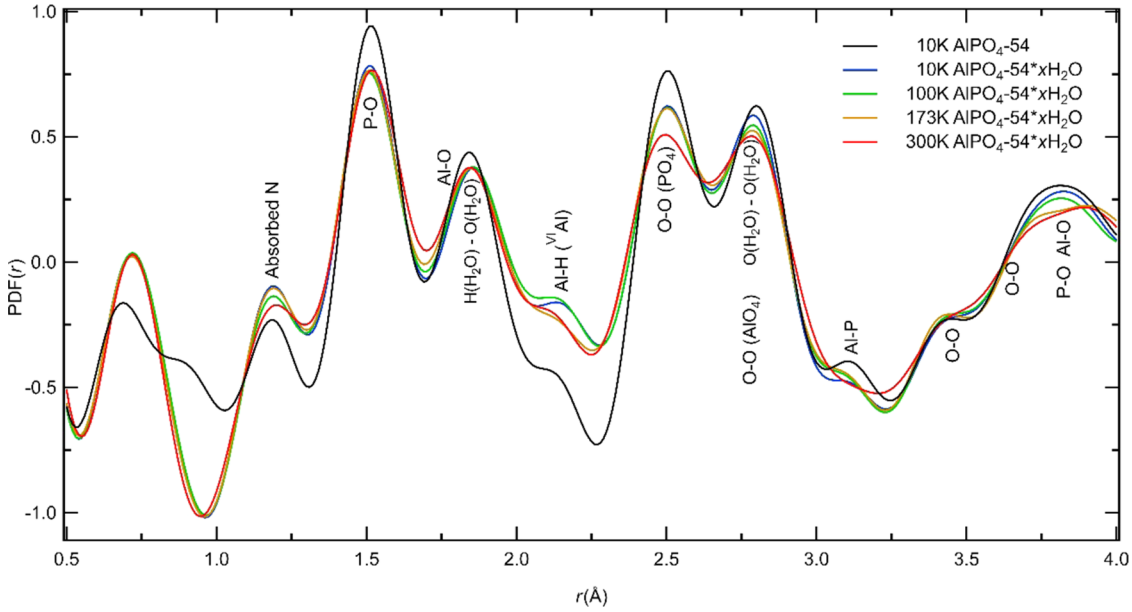

Figure 2. Pair-distribution function PDF(r) values of $AlPO_4$-54·xH_2O at T = 300, 173, 100, and 10 K and of $AlPO_4$-54 at T = 10 K.

strong interaction with the $AlPO_4$ framework that they are nearly immobile,[15] in agreement with ab initio calculations in which a few water molecules were found to be "framework molecules" as they are connected to $AlPO_4$ by a short Al−O bond.[38] Upon cooling, the water molecules located at the pore vicinity region (OW3, OW4, OW6, and OW8; see the SI, Tables S2, S3, and Figure S1), here termed proximal water, presented ADPs 2−3 times larger than those of O atoms belonging to the $AlPO_4$ structure. In the pore vicinity sites, water molecules form hydrogen bonds (HBs) with the O atoms of the water molecules located in the 6-fold Al.

Figure 1 (top) shows the refined structures of $AlPO_4$-54·xH_2O at T = 135, 100, and 50 K, illustrating the AlO_4, AlO_6, and PO_4 polyhedra and the positions of the O atoms of confined water (circle size represents the water O ADP at 50% probability). As can be observed, the space group $P6_3$ of the zeolite framework induces a 6-fold arrangement of water molecules in the pore.

The simulated structures in Figure 1 (bottom) correspond to simulated density maps of the O atoms of water. Upon decreasing the temperature with respect to the previous study limited to 173 K,[15] both the experimental (at T = 135, 100, and 50 K) and simulated (at T = 173, 110, and 10 K) structures show an increase in water ordering and site occupancies at the pore wall. The O atoms of water in the vicinity of the pore surface exhibit similar ADP to those of the O atoms in ice,[41] whereas the ADP values increase toward the pore center. The bridging angles do not change significantly upon cooling (Table S5), which is in agreement with the observation of no major change in the a and c lattice parameters with T (Table S1). The higher ADP values (experimental) and densities (simulated) observed for inner

https://doi.org/10.1021/acs.jpcc.1c01254
J. Phys. Chem. C XXXX, XXX, XXX−XXX

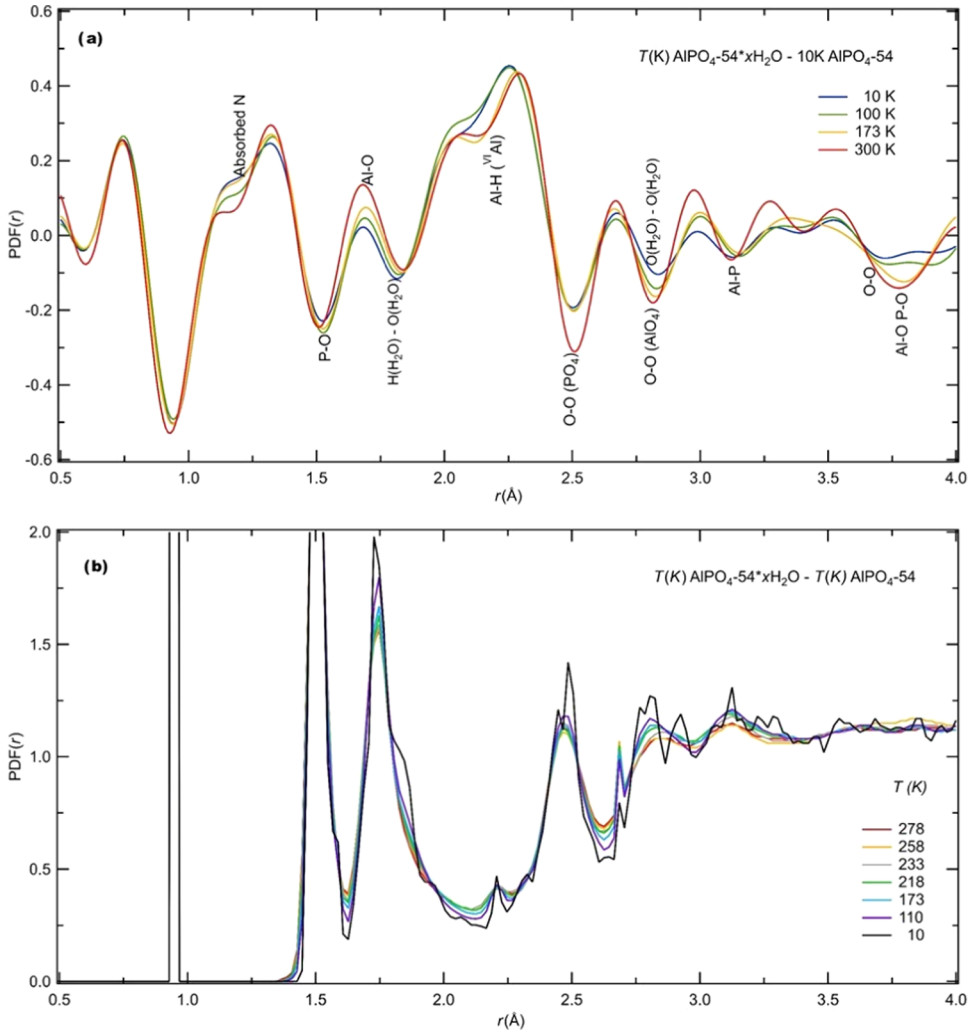

Figure 3. Experimental (a) and simulated data by MD calculations (b) differences of pair-distribution functions PDF(r) between $AlPO_4$-54·xH_2O at T = 300, 173, 100, and 10 K and its dehydrated form ($AlPO_4$-54) at T = 10 K.

water at all studied temperatures indicate a more disordered arrangement when compared to proximal water.

3.2. Pair-Distribution Function from Powder Neutron Scattering. Pair-distribution function—PDF(r)—data obtained from neutron scattering on $AlPO_4$-54·xH_2O provide information on the local structure of nanoconfined water upon cooling. At low temperature, the PDF(r) features tend to become narrower and have a higher amplitude due to the lower Debye−Waller (DW) factors. However, significant changes in peak intensities and positions should reflect structural changes. Figure 2 shows the pair-distribution function PDF(r) values of $AlPO_4$-54·xH_2O at T = 10, 100, 173, and 300 K and its dehydrated phase ($AlPO_4$-54) at T = 10 K. Both the data for the hydrated and dehydrated phases were normalized to the total sample mass illuminated by the beam. Assignment of the peaks can be obtained by comparison with single-crystal XRD data from this and previous studies.[15,18] Distances above 4 Å are somewhat more difficult to assign due to the overlap of several contributions; here, we present only the shorter distance region (<4 Å). At 1.51, 1.76, 1.8−2.0, 2.5, and 2.8 Å, typical framework intra-polyhedral distances from P−O, Al−O (tetrahedra), and Al−O (octahedra), respectively, are found. The intertetrahedral Al−P distance across the bridging angle is observed at 3.11 Å. Above 3.4 Å, several intertetrahedral distances are observed and overlapped, such as O−O, P−O, and Al−O. The peak at 2.14 Å is attributed to the Al−H distances involving the 6-fold Al. At 1.82 and 2.8 Å, the hydrogen bond (HB) and O−O distances from the pore water, respectively, are observed. The peak at 1.18 Å is attributed to a residual amount of adsorbed N_2[42] from the cryostat atmosphere at the zeolite surface. The PDF(r) of $AlPO_4$-54·xH_2O shows changes in the $AlPO_4$ structure as the temperature decreases. Here, we will focus on changes concerning nanoconfined water. Upon cooling, there is a clear sharpening of several peaks in the PDF(r), and an increase in the number of O atoms bonded via H-bonds with a typical distance of 2.8 Å; see Figure 2.

For the sake of clarity, we subtracted from the PDF(r) of $AlPO_4$-54·xH_2O at T = 10, 100, 173, and 300 K its dehydrated phase at T = 10 K; the result is shown in Figure 3a. From the PDF(r) difference, we observe that, upon decreasing the temperature, the HB (at around 1.82 Å) shifts toward lower values, which is consistent with a strengthening of the H-bond network. As aforementioned, in the $AlPO_4$-54·xH_2O structure, one-third of the aluminum cations are octahedrally coordinated due to the presence of two H_2O molecules in their coordination sphere, one of which forms strong hydrogen bonds with the free water in the pore, while, at 300 K, no

https://doi.org/10.1021/acs.jpcc.1c01254
J. Phys. Chem. C XXXX, XXX, XXX−XXX

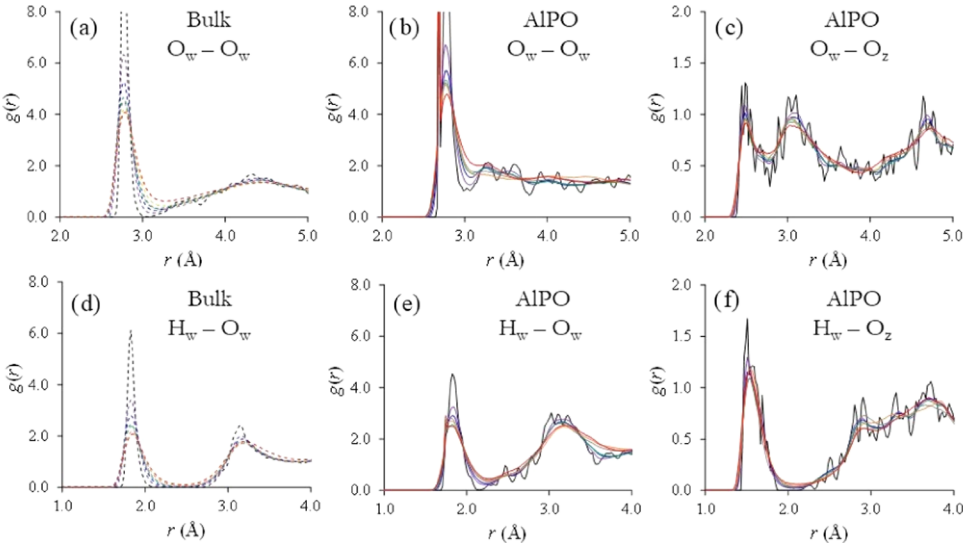

Figure 4. Pair-distribution functions $g(r)$ as obtained from grand canonical Monte Carlo simulations for bulk water and water confined in $AlPO_4$-54·xH_2O at different temperatures: T = 10 (black), 110 (purple), 173 (blue), 218 (green), 233 (gray), 258 (orange), and 278 K (red). Different contributions to the total pair-distribution function are shown (from the top, left to bottom, right): O_w−O_w for bulk water, O_w−O_w for confined water, O_w−O_z for confined water, H_w−O_w for bulk water, H_w−O_w for confined water, H_w−O_z for confined water where O_w, O_z, and H_w denote the O atom of water, the O atom of the zeolite, and the H atom of water, respectively.

hydrogen bonds are formed with the second coordinated water.[43] Figures 2 and 3a show a shift and a sharpening of the peak at 2.14 Å for temperatures lower than 173 K. Such a shift indicates changes in the local structure of the octahedral environment of Al. Concerning the Al−H intraoctahedral distance (Al−O−H), the slight increase in the peak intensity and the shortening of the Al−H intraoctahedral distance (Al−O−H) suggest structural changes in the Al−H environment. In Figure 3b, the simulated PDF(r), obtained by MD calculations, is shown for each temperature T, where PDF(r) is the difference of pair-distribution functions PDF(r) between $AlPO_4$-54·xH_2O and its dehydrated form ($AlPO_4$-54) at the same temperature. Comparing experimental and simulated data, we observe that the main features are present in both data sets. The molecular simulation results in Figure 3 and Figure 1 show noticeable differences with some of the experimental data, which may be due to the employed force field. Concerning the changes in nanoconfined water, both experimental and simulated data (Figure 3b) show a clear shift and an increase in intensity at around 1.82 Å, which is consistent with a strengthening of the H-bond network. At around 2.8 Å, the peak shifting and again the intensity increase observed in the simulated data indicate a structuring of confined water on cooling. Such a trend seems less evident in the experimental data.

For comparison, the PDF obtained by X-ray scattering measurements on water confined in a bioactive glass (5.9 nm pore diameter) also presented a shift to shorter distances and an intensity increase of the pair correlation pick at about 2.8 Å on lowering the temperature.[14] Such a study indicates that the interfacial pore water network is strongly distorted and tetrahedral-like due to the interactions between water and the amorphous silica pore surface. For water confined in the nanopores of $AlPO_4$-54·xH_2O, a different trend is observed: upon cooling, an increase of the orientational order of water molecules strongly bonded with the zeolite framework is observed, while the typical O−O distances among pore water molecules decrease.

3.3. GCMC Simulations: Radial Distribution Functions and Hydrogen Bonding. GCMC simulations were used to assess the arrangement of water molecules confined in $AlPO_4$-54·xH_2O at different temperatures. Figure 4 shows various simulated pair distributions functions $g(r)$ for bulk (Figure 4a,d) and confined water (Figure 4b,c,e,f) at T = 10, 110, 173, 218, 233, 258, and 278 K. Different contributions to the total pair-distribution function are shown as they allow the structure of confined water to be identified. In particular, these contributions were chosen to unravel the hydrogen bonding between water molecules (water/water) and between water molecules and the host zeolite (water/$AlPO_4$). As in the case of bulk water, confined water forms a hydrogen-bond network between water molecules, which becomes more ordered upon decreasing the temperature T (i.e., with correlation peaks in the $g(r)$ functions that have an amplitude/width ratio that increases with decreasing T); these hydrogen bonds correspond to the strong peak at about $r \sim 1.9$ Å, whose amplitude increases with decreasing T (Figure 4d,e). Interestingly, the proximal water also forms a pseudo-hydrogen-bonded network with the O atoms of the zeolite framework as evidenced by the peak—located at a similar distance—in the $g(r)$ between the H atoms of water and the O atoms of the $AlPO_4$-54 structure; see Figure 4f. However, this peak is less pronounced than that between water molecules (Figure 4e), therefore suggesting that ordering in confined water remains mostly driven by water−water interactions (despite the strong hydrophilicity of the zeolite structure). In this respect, it should be noted that direct quantitative comparison between the water/zeolite and water/water correlation peaks cannot be established. However, their integral relates to the number of neighboring O atoms (either from the zeolite or from other water molecules) so that these peaks do reflect the role of specific intermolecular interactions in the structuring of confined water. A strong peak is observed at $r \sim 2.7$ Å; see Figure 4b. This peak arises from the fixed O_w, as previously commented, i.e., from the water linked to one-third of the aluminum cations, which are octahedrally coordinated due to the presence of two H_2O molecules in

https://doi.org/10.1021/acs.jpcc.1c01254
J. Phys. Chem. C XXXX, XXX, XXX−XXX

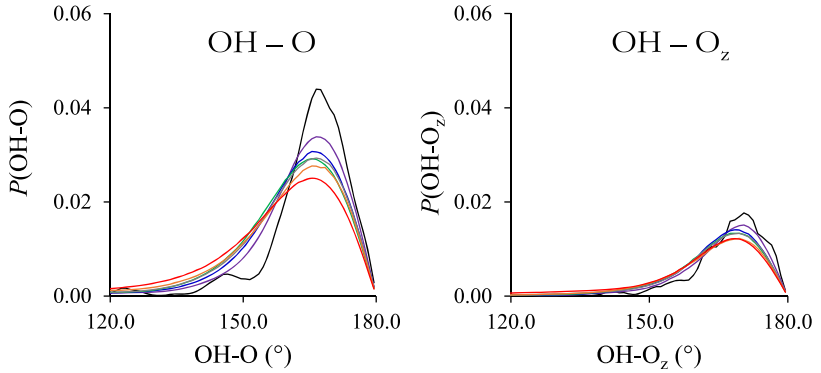

Figure 5. Distribution function of hydrogen-bonding angles as obtained from grand canonical Monte Carlo simulations for water confined in $AlPO_4$-54·xH_2O nanopores at different temperatures: T = 10 (black), 110 (purple), 173 (blue), 218 (green), 233 (gray), 258 (orange), and 278 K (red). The left figure corresponds to hydrogen bonding between confined water molecules (inner and proximal). The right figure corresponds to hydrogen bonding between proximal water molecules and the O atoms of the host zeolite. These histograms are not normalized as the number of molecules $P(\theta)d\theta$ is proportional to the number of H_2O molecules linked to a O_w (left) or O_z (right) atom with an angle between θ and $\theta + d\theta$. Therefore, the marked amplitude difference between the left and right panels indicates that there are more H_2O molecules linked to a O_w (i.e., another water molecule) than to a O_z (i.e., the zeolite framework).

their coordination sphere. Following previous studies,[15] these O_w were set at their crystallographic positions. All $g(r)$ functions for T down to 110 K suggest that inner water remains amorphous-like as no long-range positional ordering is observed. In contrast, for T = 10 K, the $g(r)$ functions for confined water suggest that water exhibits a high positional order; see Figure 4b,c,e,f. In particular, the $g(r)$ function between the O atoms of proximal water and those of the zeolite framework presents subpeaks and peaks beyond the first peak corresponding to hydrogen bonding; see Figure 4c. This result suggests that proximal water might form a more ordered arrangement as temperatures are lowered below T = 110 K in simulation runs. However, this result should be interpreted with caution. From an experimental point of view, it cannot be excluded that kinetics at such low temperatures (typically, $T \sim$ 10 K) are too slow and hinders the formation of ordered water under confinement. In this respect, we note that Monte Carlo simulations might be less prone to such issues because they rely on a sampling of the phase space using Boltzmann factors and not according to a time trajectory as in molecular dynamics simulations (even though sampling in Monte Carlo simulations is also strongly limited by low acceptance probabilities at very low temperatures). However, water dynamics has been observed to be active down to very low temperatures under extreme confinements,[44] resulting in the water ordering temperature being strongly reduced.

The pair-distribution functions $g(r)$ for confined water (Figure 4b) show a subpeak at around 3.2 Å for all studied T. This peak has been identified as the signature of HDA/HDW (high-density amorphous ice) by the TIP4P Ice model[45] and for water under pressure. Compared to the bulk, g(r) for confined water, Figure 4b, indicates a much more disordered state, which is not tetrahedral and collapsed. On fixing the first shell limit to that of bulk water (3 Å), no vanishing of the g(r) is observed at this value and an excess density of molecules is found between the two next minima 3 and 3.6 Å (red curve). The number of first neighbors for water molecules and the angle distribution between molecules in the first and second shells of neighbors were calculated (Section S3 from the SI). Note that a much smaller average number of molecules for confined water, compared to the bulk, is observed in the first shell (Figure S2), as previously observed. This coordination number for confined water depends on the local pore curvature (as flat surfaces or surfaces with curvature of the opposite sign can lead to increased coordination numbers). The hydrogen orientation distribution $P(\theta)$ for confined water (Figure S3) shows angles much more distorted and distributed, as well as a broad peak around 75° and not at 65° like in HDA. Note that this does not correspond to interstitial water molecules and can therefore be identified with the second neighbors. The hydrogen orientation distribution (Figure S3) indicates a loss of tetrahedrality (two peaks at 45 and 75°) and a broader angle distribution and distortion. The results suggest that inner water is even more distorted than an HDA network. This is in agreement with what is observed in experiments, as discussed in the following.

To further assess the structure of confined water, Figure 5 shows the distribution of hydrogen-bonding angles for water confined in $AlPO_4$-54·xH_2O nanopores at different temperatures. Both hydrogen bonding between confined water molecules and hydrogen bonding between confined water molecules (proximal water) and the O atoms of the host zeolite ($AlPO_4$ framework) are shown. These data confirm that confined water at T = 10 K is more ordered as a sharp peak is observed in these distributions together with a secondary peak (in contrast, water confined at higher temperatures does not exhibit this second peak and the distribution is much broader than for T = 10 K). For all temperatures, the main peak is located at an angle ~175°, which is very close to the value observed for bulk water. As in the case of the $g(r)$ functions, the orientational ordering of confined water is mostly driven by the water−water interactions as the peak in the angle distribution for water−water hydrogen bonding is more pronounced than that corresponding to proximal water−zeolite hydrogen bonding (water/$AlPO_4$).

3.4. INS Probe of the Generalized Density of States of Water Confined at the Nanoscale. The $AlPO_4$-54·xH_2O water vibrational spectrum consists of four main bands: the connectivity band (85−150 cm^{-1}), the librational band (300−1200 cm^{-1}), the bending band (around 1629 cm^{-1}), and the stretching band (2500−3900 cm^{-1}). Band assignments for the $AlPO_4$-54·xH_2O zeolitc water are given in Table 1.[15,16,20,21,46,47] The different spectral regions are experimentally studied with different techniques and will be discussed in

https://doi.org/10.1021/acs.jpcc.1c01254
J. Phys. Chem. C XXXX, XXX, XXX−XXX

Table 1. Band Assignments for $AlPO_4$-54·xH_2O Zeolitc Water at Ambient Pressure and Temperature[15,16,20,21,46,47]

wavenumber (cm^{-1})	assignment	label
3559	O−H stretch trimers, dimers, monomers	ν_{OH3}
3345	O−H stretch intermediate coordination	ν_{OH2}
3149	O−H stretch tetrahedral H-bonds	ν_{OH1}
1628	HOH bending	HOH
940	librational axis *x*—wagging	ω_3
737	librational axis *z*—twisting	ω_2
545	librational axis *y*—rocking	ω_1
126	connectivity H-bond	νHB_3
116	connectivity H-bond	νHB_2
109	connectivity H-bond	νHB_1

the current and the next section. In particular, the connectivity band and O−H stretching were investigated by IR and will be presented in Section 3.6.

Incoherent neutron scattering is a unique probe of individual motions and vibration properties of hydrogen due to its high incoherent cross section, typically 2 orders of magnitude larger than in other elements.[48] Since vibrations involving hydrogen dominate the incoherent inelastic neutron scattering spectrum, INS can selectively probe the vibrational dynamics of water nanoconfined in zeolite porous and other minerals. Meanwhile, the contribution coming from the framework of the host material should also be considered. The contribution to the total intensity coming from the zeolite framework is therefore mainly incoherent due to the two H_2O molecules in the Al octahedra. For a sample with structural water only (x = 0.67, no H_2O in the pore), corresponding to 12.06 H_2O molecules per unit cell, the total cross sections are $\sum_{coh} \approx 484.55$ barn and $\sum_{inch} \approx 1936.17$ barn. On the other hand, for a dehydrated material, the number of H_2O molecules per unit cell drops to 4.5, and 2.16, respectively, for a sample exposed to primary and secondary vacuum.[20] This gives rise to total cross sections per unit cell for a sample exposed to primary vacuum of $\sum_{coh} \approx 425.99$ barn and $\sum_{inch} \approx 722.64$ barn, and $\sum_{coh} \approx 407.87$ barn and $\sum_{inch} \approx 347.02$ barn for a sample exposed to secondary vacuum. The crystal structure of hydrated $AlPO_4$-54·xH_2O at ambient condition, where x = 2.14,[20,22] counts 38.52 H_2O molecules per unit cell [$Al_{18}P_{18}O_{72}$·38.52H_2O]. Consequently, the total coherent and incoherent cross sections per unit cell for a hydrated $AlPO_4$-54·xH_2O are $\sum_{coh} \approx 689.5$ barn and $\sum_{inch} \approx 6183.6$ barn, respectively. Figure 6a shows a comparison between the INS spectrum of the $AlPO_4$-54·xH_2O from 172 to 3900 cm^{-1} at T = 10, 173, 235, and 293 K and its respective dehydrated phase ($AlPO_4$-54) at T = 10 K. The comparison shows that the contribution coming from the zeolite framework is very low, representative of a structure with fewer H_2O molecules in the Al octahedra. As will be discussed in the next sections, and already reported in the SC-XRD results, the zeolite framework does not show significant changes on cooling.

From the INS spectra of $AlPO_4$-54·xH_2O (Figure 6a), three main regions typical of specific water vibrational modes can be distinguished. In the region from 300 to 1200 cm^{-1}, intermolecular librational modes (frustrated rotational oscillations) are present. Around ~1628 cm^{-1}, the HOH bending

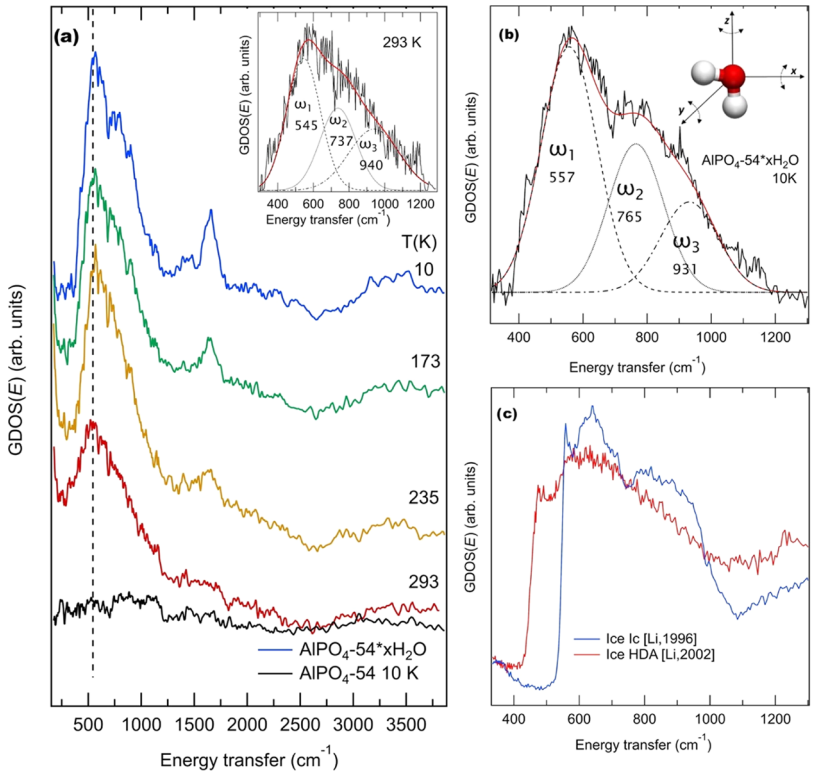

Figure 6. (a) INS spectra of $AlPO_4$-54·xH_2O (colored) at T = 10, 173, 235, and 293 K and dehydrated (black) $AlPO_4$-54 at T = 10 K. Inset (a): librational band for $AlPO_4$-54·xH_2O at T = 293 K together with the deconvoluted Gaussian components (dashed lines) corresponding to the three librational modes around the three symmetry axes of water molecules (see inset (b); H, white sphere; O, red sphere). (b) INS spectra of $AlPO_4$-54·xH_2O at T = 10 K together with the deconvoluted Gaussian components (dashed lines). (c) Normalized INS spectra comparison between ice Ic (blue line) and high-density amorphous ice (HDA, red line), reproduced with permission from refs 50, 51.

https://doi.org/10.1021/acs.jpcc.1c01254
J. Phys. Chem. C XXXX, XXX, XXX−XXX

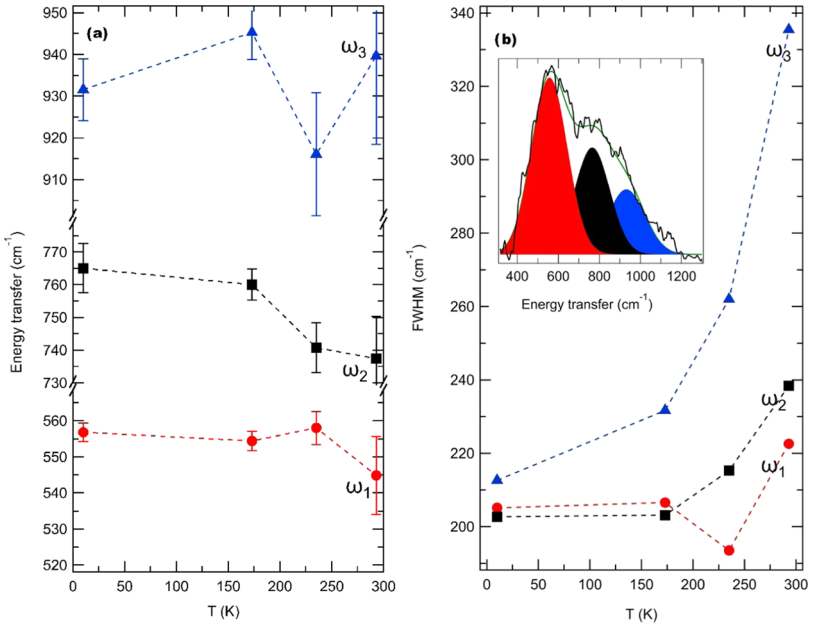

Figure 7. (a) Intermolecular librational mode frequencies and (b) full width at half-maximum (FWHM) of the librational sub-bands at selected temperatures. Inset (b): the librational band with the three components at 10 K.

mode is visible. At higher energies, from 2500 to 4000 cm^{-1}, the vibrational modes are assigned to OH stretching. The stretching bands are poorly measured on an inverse geometry spectrometer (as LAGRANGE) due to the presence at high energies of a high Debye−Waller factor (even at low temperatures). For this reason, the OH band is overdamped and in addition shows multiphonon contributions.[34,35,49] Conversely, the $AlPO_4$-54·xH_2O INS spectrum shows a well-visible band in the region 300−1200 cm^{-1}, corresponding to the librational bands of water molecules and which has not been probed by other spectroscopic techniques (such as Raman and IR), as this region is typically dominated by the zeolite framework modes. Since the highest energy-part of the INS spectra (>2000 cm^{-1}) did not show significant features, and can be better probed with other spectroscopic techniques, we focus the present analysis mainly in the region from 250 to 1250 cm^{-1} (31−156 meV), with further comments on the bending mode, located at 1628 cm^{-1}.

3.4.1. Librational Region. The librational motions of water about the three principal axes of an isolated molecule are referred to as the wagging, twisting, and rocking vibrations, with only two of these being IR- and Raman-active. In contrast, the three libration modes are observed by neutron scattering. The three symmetry axes are defined as follows: the y and z axes are the molecule plane; while the x axis is perpendicular to the plane (Figure 6b, inset). The observed sub-bands ω_1, ω_2, and ω_3, Figure 6a inset, correspond to the librational modes around the axes y, z, and x, respectively.[46,52]

These librational bands are very sensitive to variation in the H-bond network, and in general, the peak frequency increases and peak width decreases when rotations are more restricted due to H-bonding.[31,32] As a consequence, in Ice, the librational bands are observed at higher frequencies when compared with water[53] as a more structured hydrogen-bond network produces a stronger restoring force. In bulk water, the librational band evolves strongly from a broad band in the liquid phase to a sharp and intense structure in hexagonal ice.[50]

To follow the temperature evolution of the librational band, the dashed vertical line in Figure 6a is a guide to the eye fixed at the ω_1 sub-band position at T = 293 K. At the lowest temperature (T = 10 K), the INS spectrum shows some changes in the librational band with respect to room temperature: an intensity increase and two better-defined maxima are observed (Figure 6a,b). As in the PDF(r), upon cooling, the INS spectra are expected to increase in intensity due to the Debye−Waller (DW) factor. On the other hand, a better-defined maximum at lower temperature is a clear signature of a more ordered structure. In bulk water, the librational band evolves strongly from a broad band in the liquid phase to a sharp and intense structure in hexagonal ice.[50] Here, the observed changes suggest that at low T (10 K) there is an increased contribution from an ordered arrangement with the number of H-bonds increasing to a total average somewhat less than the four per molecule (like ice).[50] It must be remarked that the spectra of Ic, Ih, and low-density amorphous (LDA) ices are almost superimposed in the librational region.[50] Indeed, the crystalline (Ic and Ih) and amorphous ices (LDA) have similar density and a coordination number of about 4, with their local structures being basically the same.[50] Conversely, the INS spectrum from the librational band of the high-density amorphous ice (HDA)[50] strongly differs from those of Ic, Ih, and LDA ices (Figure 6c). HDA shows a general broader band, which starts at lower energy and presents less intense and broader modes at higher energy. Such features in HDA's librational mode are linked to inter-penetrated structures, as present in ices VII and VI. Figure 6b presents the INS spectra of the librational band from $AlPO_4$-54·xH_2O at T = 10 K, in comparison with Figure 6c, which presents the librational band from a crystalline ice Ic and high-density amorphous ice (HDA) and that are shown with the same scale. The librational band of the zeolite-nano-confined water at the lowest T (10 K) shows common features with both bulk ices, HDA, and Ic, although overall the modes are slightly shifted to lower frequencies. Indeed, it presents two sharp maxima similar to those observed in the ice Ic spectrum

https://doi.org/10.1021/acs.jpcc.1c01254
J. Phys. Chem. C XXXX, XXX, XXX−XXX

and, similar to HDA, a broad high-frequency mode (ω_3) at frequencies of about 900−1000 cm^{-1}. In addition, similar to the HDA, there is a structure extending at lower frequencies with a shoulder at around 474 cm^{-1}. This observation supports once again the hypothesis that at the lowest T the arrangement of nanoconfined water molecules may be a superposition of a locally ordered arrangement (as indicated by the two well-defined maxima), together with a high-density disordered arrangement (as indicated by its broad lower energy contribution). This scenario is in agreement with SC-XRD, GCMC, and PDF results.

A detailed analysis of the librational band can be performed by describing with several overlapping Gaussian components after removing the slowly rising linear background.[21,47,54,55] This technique (also used for the IR modes, Section 3.6) was recently applied successfully to other $AlPO_4$ molecular sieves and zeolites to evidence the correlation between structural and vibrational properties.[21,47,55] A complete description can be found in previous works.[21,47,55] For clarity, we only present the water band region prior to the background removal together with the fitted Gaussians and their assignment. Such a fit provides a sound tool to quantitatively account for the changes in water modes, although the present Gaussian and background fit is not unique. Figure 7 shows the temperature dependence of the INS librational sub-band frequencies and their respective full width at half-maximum (FWHM) values. The decrease of the librational width, compared to bulk water, is attributable to the ordering arrangements of hydrogen atoms, as observed in ice.[56,57] The librational sub-band frequency can be roughly correlated with the strength of the hydrogen bonding, while the width is inversely related to the robustness of the network. Upon decreasing T, both lowest energy libration sub-bands (ω_1 and ω_2) are observed to shift to higher wavenumbers, while a decrease in the FWHM of the three modes (Figure 7) is observed. The shift in frequency is an indication of the formation of a network with stronger HB upon lowering T, which is in agreement with the PDF results, while the narrowing suggests more robust bonds. The highest energy mode (ω_3) presents stronger changes: the FWHM strongly decreases with temperature, while its frequency does not show a particular trend.

3.4.2. Bending Region. The INS spectrum also shows evidence of temperature effect on the HOH bending mode. This single component band increases in intensity upon cooling, due to the DW factor, and shifts to higher frequencies, Figure 6a, varying from ∼1628 cm^{-1} at room temperature (Table S1) to ∼1686 cm^{-1} at T = 10 K. This variation is similar to the one observed in bulk water during crystallization,[54] and the nonevolving single Gaussian shape is an indication that the bending mode is not sensitive to the modifications of connectivity of the nanoconfined water.

3.5. Ab Initio Molecular Dynamics Simulations. Simulations by AIMD were performed for the $AlPO_4$-54·$x$$H_2O$ system to support and better interpret the experimental results. The atomic contributions to the density of states of the H atoms g_H (E) are determined for water in various locations. In particular, both structural (linked to ^{VI}Al) and confined (nano unidirectional pore) water, in which only the oxygen atoms from H_2O are considered, were included in the model. The density of states values for two types of H have been labeled: those in H_2O coordinated to the ^{VI}Al and those to the nanoconfined pore water, named H-coordinated (structural) and H-pore (inner and proximal), respectively. Figure 8 shows

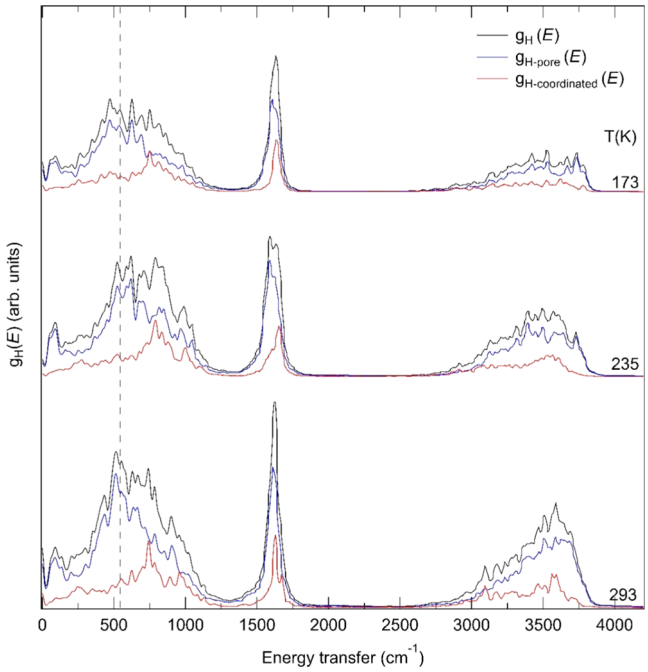

Figure 8. Comparison of the calculated, $g_{H\text{-coordinated}}$ (E) and $g_{H\text{-pore}}$ (E), with the total hydrogen density of states g_H (E), of $AlPO_4$-54·$x$$H_2O$ for T = 173, 253, and 293 K.

the comparison of the calculated, $g_{H\text{-coordinated}}$ (E) and $g_{H\text{-pore}}$ (E), and the total hydrogen vibrational density of states, g_H (E), of $AlPO_4$-54·$x$$H_2O$ for T = 173, 235, and 293 K. Four main bands are observed, as described previously: the connectivity band (85−150 cm^{-1}), the librational band (300−1200 cm^{-1}), the bending band (around 1629 cm^{-1}), and the stretching band (2500−3900 cm^{-1}). Here, we will focus on changes concerning the librational band, while further comments on the connectivity and stretching bands appear in the next section (IR at low T). The dashed vertical line is, here again, a guide to the eye and represents the ω_1 sub-band position from the INS results at T = 293 K. AIMD shows that changes in the librational band are dominated by the adsorbed confined water (inner and proximal). A red shift of the librational lower edge, together with a variation in intensity, is observed on decreasing the temperature from T = 235 to 173 K. Such a shift and its respective change with temperature in the librational band shape are observed also at the INS spectrum, Figures 6a and 7, and involves mostly both lowest sub-bands (ω_1 and ω_2, Figure 7), which shows a good agreement between INS and AIMD. Such a shift (see the dashed line guide) and the overall librational intensity change suggest some modification in the nanoconfined water network. In the following, these strong indications of dynamic transitions will be confronted with the IR results.

3.6. Far- and Mid-IR Absorption at Low Temperature. Far- and mid-IR spectra of water confined in $AlPO_4$-54·$x$$H_2O$ nanopores were measured in a wide range of temperatures to complete the water vibrational information obtained previously. The infrared spectra from $AlPO_4$-54·$x$$H_2O$ are dominated by contributions from molecules located in the pores, as shown in Figure S4 (Supporting Information). From single-crystal XRD results (Section 3.1) and previous IR studies,[15] we know that changes in the $AlPO_4$-54·$x$$H_2O$ structural framework are negligible upon cooling; therefore, changes in IR absorption observed when lowering the

https://doi.org/10.1021/acs.jpcc.1c01254
J. Phys. Chem. C XXXX, XXX, XXX−XXX

temperature can be linked to the evolution of the nanoconfined water.

The present IR measurements are here only shown between 50 and 150 cm^{-1} and between 2000 and 4000 cm^{-1}, the intermediate energy range (150−1800 cm^{-1}) being masked by strong modes from the structural framework. A detailed description of the IR structural framework modes in the $AlPO_4$-54 can be found elsewhere.[21] Thus, the present IR spectra only probe part of the connectivity (H-bond stretching) and the O−H intramolecular water vibration. The mid- and far-IR spectral profiles of the vibrational modes of water confined in the $AlPO_4$-54·xH_2O nanopores were obtained by the same technique described in the previous section (see Section 3.4 INS).

3.6.1. OH Stretching Band. Figure 9a shows the IR spectra of nanoconfined water in $AlPO_4$-54·xH_2O in the region of the

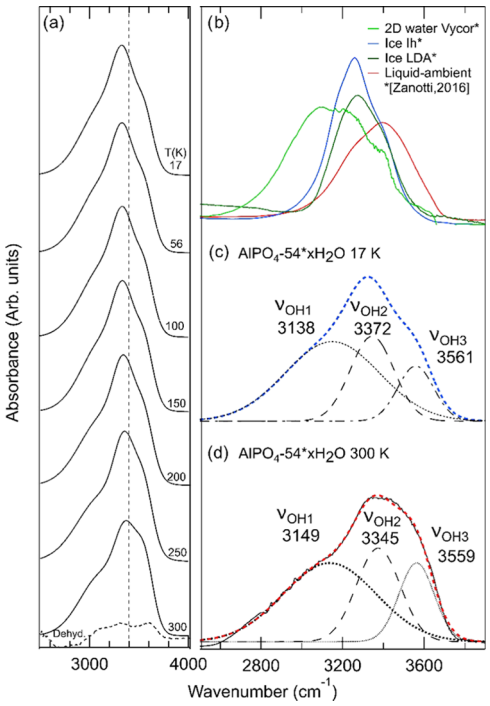

Figure 9. (a) OH stretching band of $AlPO_4$-54·xH_2O at selected temperatures and the dehydrated $AlPO_4$-54 at 300 K (dashed line). (b) The spectra of the water monolayer in Vycor*,[58] hexagonal ice* (Ih, blue line),[58] low-density amorphous* (LDA, green line),[58] and bulk liquid water (red line) are shown for comparison. (*) Reproduced with permission from ref 58. (All spectra were measured on the AILES beamline.) (c) and (d) OH band of $AlPO_4$-54·xH_2O measured at 17 and 300 K, respectively, with deconvoluted Gaussian components (dashed lines).

OH stretching band measured at various temperatures between 300 and 17 K. For all temperatures, this band is extremely wide in energy, covering continuously the range between 2500 and 3700 cm^{-1}. At ambient T, the OH stretching band presents three broad sub-bands at about 3149, 3345, and 3559 cm^{-1}, named νOH_1, νOH_2, and νOH_3 in the following. The dashed vertical line is a guide to the eye and represents the νOH_2 sub-band position at T = 300 K. The contribution of these modes is negligible in the equivalent dehydrated state, as shown by g_H (E), Figures 8 and 9, and by previous studies on $AlPO_4$-54.[21]

Water molecules can establish bonds with other confined water molecules (such as inner−inner and/or proximal−proximal water) and with proximal water and the $AlPO_4$-54·xH_2O framework.[47] In analogy with the measurements by Zanotti et al.,[58] presented in the inset of Figure 9b, the first layer of water molecules in direct contact with the hydrophilic surface gives rise to a defined OH stretching mode around 3150 cm^{-1} (νOH_1), revealing that the H-bonds involved are significantly stronger than the corresponding H-bonds observed in the lowest energy component of bulk water (see ice or liquid water OH; Figure 9b).

The other two higher-frequency substructures (νOH_2 and νOH_3) are assigned to populations of pore water molecules belonging to two distinct networks designated as inner and proximal water. These modes appear at very high frequency, suggesting that the establishment of the hydrogen bonds is partially hindered due to the small size and curvature of the pores.

Figure 9b presents the OH stretching mode of water in various conditions: a monolayer of water in porous Vycor (where all four bonds are established, lighter green line); the bulk liquid water (red line); hexagonal ice (Ih, blue line); and low-density amorphous ice (LDA, darker green line). Figure 9c and d presents the deconvoluted modes of water in $AlPO_4$-54·xH_2O measured at 17 and 300 K, respectively. The comparison of these modes with other water presented in Figure 9b suggests the presence of different water networks coexisting at the lowest T: (i) one layer in direct contact with the zeolic pore walls with strong H-bonds established with the zeolite framework and giving rise to the shoulder at 3150 cm^{-1}, together with (ii) two H-bond networks, likely associated with proximal−inner and inner−inner water populations, absorbing between 3300 and 3700 cm^{-1}, and showing, respectively, a vibrational behavior similar to low-density amorphous ice (proximal water) and one closer to liquid water (see the comparison in Figure 9b,c). The observation of two different networks coexisting within the nanopores is in agreement with the deductions from the libration studied by INS and supported by the SC-XRD results.

3.6.2. Low-Energy Connectivity Band. Figure 10a shows the evolution as a function of temperature of part of the connectivity of water in $AlPO_4$-54·xH_2O as well as the spectrum of the dehydrated phase $AlPO_4$-54 at 17 K. As stated previously, the connectivity is possibly extending in a wider range than presented here, but the higher energy range is masked by structures from the confining system. At ambient T, this low-energy band presents three features at around 109, 116, and 126 cm^{-1}, named νHB_1, νHB_2, and νHB_3 in the following. These modes are not observed in the equivalent dehydrated state, as shown by its dehydrated spectra, Figure 10a, and by the g_H (E), Figure 8. The vertical line is a guide to the eye for the νHB_2 sub-band position at T = 300 K. In agreement with the OH band deductions, we expect different water networks with (i) H-bonding established between proximal water molecules and the $AlPO_4$-54·xH_2O framework[47] and (ii) H-bonding established among confined water molecules of both proximal and inner water.

Based on the g_H (E) calculations, Figure 8, and by comparison with measurements of water confined in Vycor[58] and in zeolites,[47] the strong HB between proximal water molecules and the pore surface is expected to give rise to a weak band extending between 120 and 250 cm^{-1}. In the present system, only its lowest frequency part is visible here and may correspond to νHB_3. The lower frequency substructures νHB_2 and νHB_1 imply weaker H-bonds and

https://doi.org/10.1021/acs.jpcc.1c01254
J. Phys. Chem. C XXXX, XXX, XXX−XXX

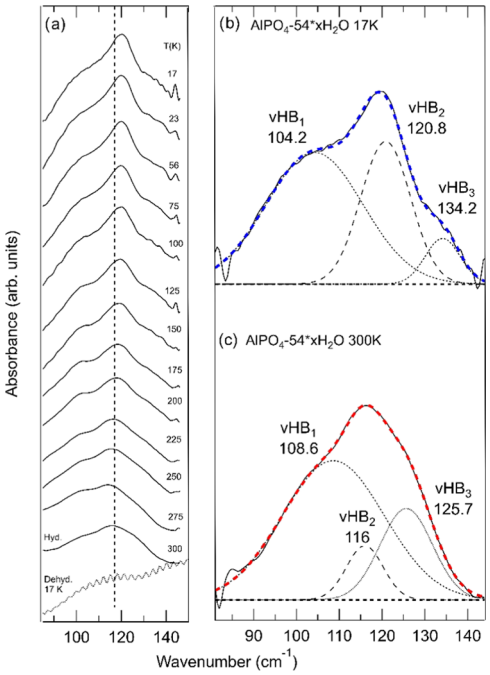

Figure 10. (a) Part of the low-energy spectra of $AlPO_4$-54·xH_2O at selected temperatures (full line) and the dehydrated $AlPO_4$-54 at 17 K (dot line). (b) and (c): Part of the connectivity band from the difference between hydrated and dehydrated samples measured at 17 and 300 K with deconvoluted Gaussian components (dashed lines).

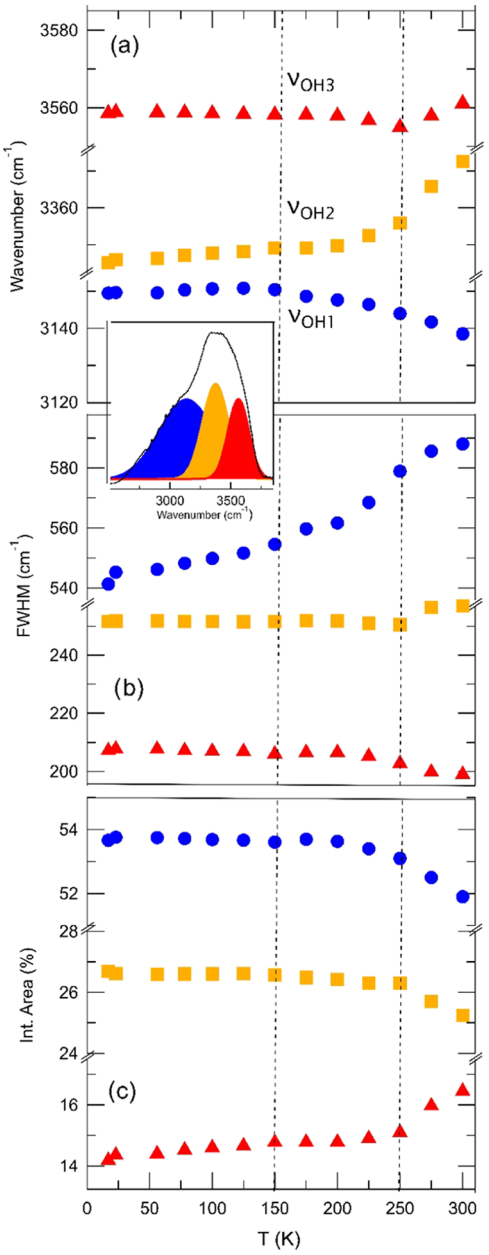

Figure 11. $AlPO_4$-54·xH_2O OH three component modes as a function of temperature (a): frequency of νOH_1, νOH_2, and νOH_3 (b): full width at half-maximum (FWHM) and (c): integrated area. Errors are smaller than the symbol size. Inset: the OH band with the three components at 300 K.

can consequently be assigned to H-bonds from water−water interactions belonging to proximal and inner water, respectively. This is in good agreement with the $g_H(E)$ calculations for confined water predicting connectivity structures under 100 cm^{-1}.

The temperature evolution of the average frequencies of both the OH stretching and the connectivity bands has been derived by a best fit employing a 3 Gaussian model, shown in Figures 9c/d and 10b/c. Figure 11a reports the temperature dependence of the three Gaussian frequencies, with their respective FWHM (Figure 11b) and integrated area (Figure 11c) for the OH stretching band, while Figure 12 presents equivalent parameters for the connectivity band.

Changes in the temperature evolution of water vibrational modes are observed at two main temperatures: 150 and 250 K (Figure 10a). Similar changes were observed after cooling down the single monolayer of water at the surface of the larger pores of Vycor glass,[58] at 160 and 250 K, and for water confined in a porous silica substrate (MCM-41/C10), with T depending on the applied pressure.[10] In both studies, these changes were associated with "dynamical transitions", related to modifications of the HB network. To quantify these changes, we analyzed the frequency and intensity evolution of the modes (Figures 11 and 12).

(i). From T = 300 to ∼250 K (RT). The frequencies of the two OH sub-bands, νOH_2 and νOH_3, decrease with temperature (see Figure 11a,b), with the νOH_2 frequency lowering more, indicating an evolution toward a stronger HB network at lower T. The peak integrated area of the νOH_2 band increases when lowering the temperature at the expense of the population of the νOH_3 band. This evolution is associated with inner water evolving to a denser liquid.[15,58] In contrast, ν_{OH1} shifts to lower energies, suggesting a continuous increase in the strength of the H-bonds between proximal water and the pore walls, which is confirmed by the evolution of the νHB_3 mode.

(ii). From T = 250 to ∼150 K. Both inner and proximal water show changes in their network. From 250 K, νOH_2 and νOH_3 show changes indicating a less percolative network. The νOH_1 frequency markedly increases while its FWHM decreases coherently with the proximal water population evolving toward shorter distances between water molecules and the walls, in agreement with a more ordered network of water molecules. Meanwhile, νOH_2 and νOH_3 show opposite evolution in frequency. This latter behavior is associated

https://doi.org/10.1021/acs.jpcc.1c01254
J. Phys. Chem. C XXXX, XXX, XXX−XXX

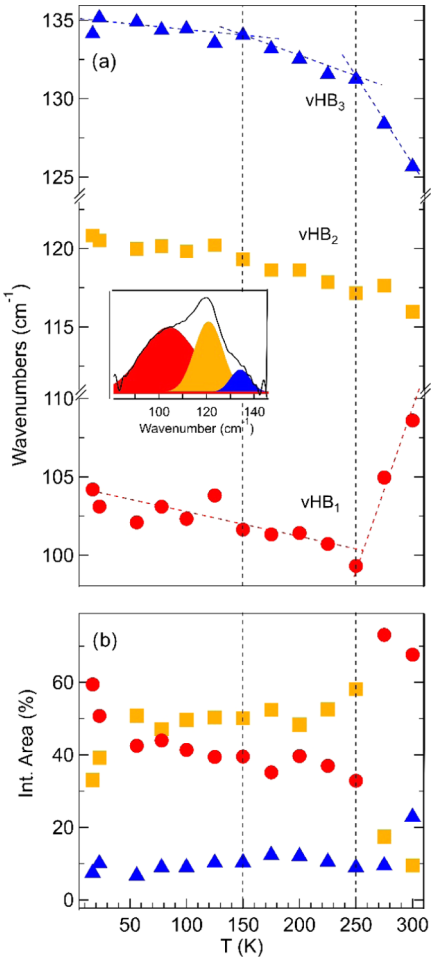

Figure 12. $AlPO_4$-54·xH_2O connectivity three component modes as a function of temperature (a): frequency of νHB_1, νHB_2, and νHB_3 (b): integrated area. Errors are smaller than the symbol size. Inset: the connectivity band with the three components at 17 K.

with the inner water population developing a more percolative water network with stronger H-bonds, as shown by the increase in frequency of both νHB_1 and νHB_2. The inner population is thus characterized by a more disordered network, with respect to both ice Ih and LDA, in agreement with a previous study.[15]

(iii). From T = 150 to ∼17 K. From 150 K, various parameters suggest only smooth changes, evidenced by small shifts in frequency for νOH_1, νOH_2, and νOH_3 modes. From 150 K, all OH widths remain constant except for the νOH_1 width, which decreases, pointing at a decreasing mobility for the proximal water. In contrast, the connectivity components νHB_1 and νHB_2 become significantly stronger, suggesting continuous strengthening of the inner water network.

This may be related to the change of the arrangement of water molecules (see Figure 12b) showing a stronger bonded structure as T decreases. The fact that the intensity of the νHB_1 band increases also indicates a possible change in the inner water density as supported by PDF analysis and GCMC simulations.

As for bulk water, shifts in the melting temperature are expected and have been experimentally observed[10,59] for water under nanoconfinement due to the Gibbs−Thomson effect.[10,60] However, such a shift depends on several factors, including pore size and pore wall properties.[61] A markedly different behavior of proximal and inner water populations is here observed, similar to what is already observed for water confined in a silica matrix (MCM system) but at much higher temperatures.[10]

In the case of MCM confined water, however, the amorphous nature of the pore promotes the existence of an amorphous nonfreezable layer of water proximal to the pore, while the higher size of the pore does not prevent the formation of ice in inner water. In $AlPO_4$-54·xH_2O confined water, no hints of ice formation are observed even at the lower investigated temperature: the smaller pore diameter shifts to lower temperatures the water freezing temperature and the hydrophilicity of the pore surface induces a clear distinct behavior of the two water populations as long as the diffusive dynamics are frozen. The long-range zeolite crystal framework may indeed contribute to the proximal water ordering, acting as an orientational template. This is in agreement with GCMC simulations, which suggests that proximal water might form ordered arrangements at lower T close to 110 K. Such a freezing in the proximal water network is consistent with an ordering of the H_2O molecules involved in hydrogen bonding with the structural water linked to the framework and may be evidenced by the strong changes in the local structure of the octahedral environment of Al below 173 K, observed in the measured PDFs.

4. CONCLUSIONS

The structure and vibrational properties of water molecules confined in unidirectional hydrophilic nanopores of $AlPO_4$-54·xH_2O were investigated at low temperatures. On cooling, from RT down to ∼250 K, two distinct water networks appear: proximal water near the pore wall and inner water at the pore center. From 250 down to ∼150 K, both proximal and inner water develop more defined local arrangements and with a distinct long-range order: while proximal water is well-ordered at the pore wall due to strong interactions with the pore surface,[15] inner water retains a disordered arrangement as strong confinements prevent the formation of a network of tetrahedrally coordinated molecules.[15]

From ∼150 down to ∼10 K, our results point to a strengthening of the water−water interactions and a densification of inner water.

While proximal water shows a continuous increase in its ordering upon cooling, inner water becomes more disordered and thus the distinction between the two networks increases. Such an ordering for proximal water is likely driven by water−water interactions despite the strong hydrophilicity of the zeolite structure. The formation of a more ordered local arrangement on cooling below ∼150 K is evidenced by the OH stretching and connectivity band evolution with temperature, as observed by IR measurements. The increase in proximal water local order is also confirmed by the PDF results and GCMC simulations, which indicate the establishment of a hydrophilic bond between proximal water and the zeolitic framework. INS results suggest an increasing mix of denser amorphous and lighter (less dense) locally ordered arrangements in water confined down to the lower T (10 K). The librational band also presents defined features arising from a lighter ordered local structure (such as Ic and/or LDA ices), embedded in a broader band arising from a disordered denser state (more similar to HDA). Both experiment and simulation results suggest an overall densification effect on cooling. The

https://doi.org/10.1021/acs.jpcc.1c01254
J. Phys. Chem. C XXXX, XXX, XXX−XXX

calculated PDF(r) shows an increased number of water molecules held at van der Waals distances (≈3.3 Å), in line with a denser state, such as HDA. Such a population of water molecules is disordered, and the presence of interstitial molecules could explain the presence of stronger, i.e., shorter HB.[45] Simulations and far-IR and INS results suggest that inner water is even more distorted than HDA, but similarly denser. Moreover, since the framework is essentially rigid (SC-XRD results show no variation in the pore size), the overall density of water must be constant. In this line, densification can only occur for the inner water, whereas the density of the proximal water must decrease to keep the overall density constant.

In conclusion, the low T experiments suggest the presence of two distinct unidirectional arrangements of water molecules in the $AlPO_4$-54·xH_2O nanochannels, whose coexistence persists at the lowest studied T. Upon cooling below 150 K, a dense arrangement of water molecules with a degree of disorder even greater than HDA develops and coexists in a less dense and highly ordered local arrangement of water molecules, whose orientational order is mainly dictated by the pore surface.

These two independent networks imply very diverse settings: one supporting mobile water with many broken H-bonds located in the center of the pores (inner water), while the other one is strongly bonded to both the interface and other water molecules (proximal water) and acts as amorphous 2D ice with very low reactivity.

■ ASSOCIATED CONTENT

Supporting Information

The Supporting Information is available free of charge at https://pubs.acs.org/doi/10.1021/acs.jpcc.1c01254.

Methods: ab initio molecular dynamics simulations; results: crystal structure refinements; GCMC simulations: refined structural analysis of confined water (PDF); far- and mid-infrared spectra

■ AUTHOR INFORMATION

Corresponding Authors

Frederico G. Alabarse − *Institut de Minéralogie, de Physique des Matériaux et de Cosmochimie (IMPMC), UMR 7590 CNRS−Sorbonne Université-IRD-MNHN, 75252 Paris, France; Elettra Sincrotrone Trieste, 34149 Basovizza, Trieste, Italy;* orcid.org/0000-0002-7375-3666; Phone: +39.337.127.0679; Email: frederico.alabarse@elettra.eu; Fax: +39.040.938.0904

Livia E. Bove − *Institut de Minéralogie, de Physique des Matériaux et de Cosmochimie (IMPMC), UMR 7590 CNRS−Sorbonne Université-IRD-MNHN, 75252 Paris, France; Dipartimento di Fisica, Università di Roma la Sapienza, 00185 Roma, Italy*; Phone: +390649923477; Email: liviaeleonora.bove@uniroma1.it; Fax: +33.1.4427.3785

Authors

Benoît Baptiste − *Institut de Minéralogie, de Physique des Matériaux et de Cosmochimie (IMPMC), UMR 7590 CNRS−Sorbonne Université-IRD-MNHN, 75252 Paris, France*

Mónica Jiménez-Ruiz − *Institut Laue-Langevin, 38042 Grenoble, France;* orcid.org/0000-0002-9856-807X

Benoit Coasne − *Univ. Grenoble Alpes, CNRS, LIPhy, 38000 Grenoble, France;* orcid.org/0000-0002-3933-9744

Julien Haines − *ICGM, CNRS, ENSCM, Université de Montpellier, 34095 Montpellier, France;* orcid.org/0000-0002-7030-3213

Jean-Blaise Brubach − *Synchrotron Soleil, 91190 Gif sur Yvette, France;* orcid.org/0000-0002-5485-5683

Pascale Roy − *Synchrotron Soleil, 91190 Gif sur Yvette, France*

Henry E. Fischer − *Institut Laue-Langevin, 38042 Grenoble, France*

Stefan Klotz − *Institut de Minéralogie, de Physique des Matériaux et de Cosmochimie (IMPMC), UMR 7590 CNRS−Sorbonne Université-IRD-MNHN, 75252 Paris, France*

Complete contact information is available at: https://pubs.acs.org/10.1021/acs.jpcc.1c01254

Notes

The authors declare no competing financial interest.

■ ACKNOWLEDGMENTS

The authors thank the Agence Nationale de la Recherche within the Blanc International program PACS (reference ANR-13-IS04-0006-01) for financing this study, and the support by the French state funds managed by ANR (project ANR-09-BLAN-0018-01) is acknowledged. The inelastic neutron scattering experiments were performed at the IN1-LAGRANGE (experiment 6-02-563; doi: 10.5291/ILL-DATA.6-02-563), and the neutron diffraction experiments were performed at D4 (experiment 6-07-10; doi: 10.5291/ILL-DATA.6-07-10), both in the Institut Laue-Langevin (ILL). The far- and mid-infrared spectroscopy experiments were performed at the AILES beamline (proposal number: 2016566) in the Synchrotron SOLEIL. The authors acknowledge the synchrotron beam time allocated for this study by the Soleil scientific proposal committee in the framework of the CNRS RECIPROCS network (project 20160753), and Pierre Fertey for assistance during the measurements at the CRISTAL beamline. The authors thank Lise-Marie Chamoreau and Dominique Granier (Réseau Rayons X et γ de l'Université de Montpellier) for helping with single-crystal X-ray diffraction measurements at 100 and 135 K, respectively. Also, the authors thank Dr. Eleonora Stefanutti for the helpful discussion on the vibrational data.

■ REFERENCES

(1) Gelb, L. D.; Gubbins, K. E.; Radhakrishnan, R.; Sliwinska-Bartkowiak, M. Phase separation in Confined Systems. *Rep. Prog. Phys.* **1999**, *62*, No. 1573.

(2) Klein, J.; Kumacheva, E. Confinement-Induced Phase Transitions in Simple Liquids. *Science* **1995**, *269*, 816−819.

(3) Deville, S.; Saiz, E.; Nalla, R. K.; Tomsia, A. P. Freezing as a Path to Build Complex Composites. *Science* **2006**, *311*, 515−523.

(4) Coussy, O. *Mechanics and Physics of Porous Solids*; Wiley: New York, 2010.

(5) Coasne, B.; Galarneau, A.; Pellenq, R. J.; Di Renzo, F. Adsorption, Intrusion and Freezing in Porous Silica: the View from the Nanoscale. *Chem. Soc. Rev.* **2013**, *42*, 4141−4212.

(6) Giovambattista, N.; Rossky, P. J.; De Benedetti, P. G. Effect of Temperature on the Structure and Phase Behavior of Water Confined by Hydrophobic, Hydrophilic, and Heterogeneous Surfaces. *J. Phys. Chem. B* **2009**, *113*, 13723−13757.

(7) Zangi, R.; Mark, A. E. Electrofreezing of Confined Water. *J. Chem. Phys.* **2004**, *120*, 7123−7130.
(8) Koga, K.; Zeng, X. C.; Tanaka, H. Freezing of Confined Water: A Bilayer Ice Phase in Hydrophobic Nanopores. *Phys. Rev. Lett.* **1997**, *79*, 5262−5265.
(9) Koga, K.; Gao, G. T.; Tanaka, H.; Zeng, X. C. Formation of Ordered Ice Nanotubes Inside Carbon Nanotubes. *Nature* **2001**, *412*, 802−807.
(10) Stefanutti, E.; Bove, L. E.; Alabarse, F. G.; Lelong, G.; Bruni, F.; Ricci, M. A. Vibrational Dynamics of Confined Supercooled Water. *J. Chem. Phys.* **2019**, *150*, 224504−224515.
(11) Dalla Bernardina, S.; Paineau, E.; Brubach, J.-B.; Judeinstein, P.; Rouzière, S.; Launois, P.; Roy, P. Water in Carbon Nanotubes: the Peculiar Hydrogen Bond Network Revealed by Infrared Spectroscopy. *J. Am. Chem. Soc.* **2016**, *138*, 10437−10443.
(12) Müller, A.; Henry, M. Nanocapsule Water-based Chemistry. *C. R. Chim.* **2003**, *6*, 1201−1208.
(13) Monet, G.; Paineau, E.; Chai, Z.; Amara, M. S.; Orecchini, A.; Jimenez-Ruiz, M.; Ruiz-Caridad, A.; Fine, L.; Rouziere, S.; Liu, L.-M.; et al. Solid Wetting-layers in Inorganic Nano-reactors: the Water in Imogolite Nanotube Case. *Nanoscale Adv.* **2020**, *2*, 1869−1877.
(14) Khoder, H.; Schaniel, D.; Pilleta, S.; Bendeifa, E.-E. X-ray scattering study of water confined in bioactive glasses: experimental and simulated pair distribution function. *Acta Crystallogr., Sect. A: Found. Crystallogr.* **2020**, *76*, 589−599.
(15) Alabarse, F. G.; Haines, J.; Cambon, O.; Levelut, C.; Bourgogne, D.; Haidoux, A.; Granier, D.; Coasne, B. Freezing of Water Confined at the Nanoscale. *Phys. Rev. Lett.* **2012**, *109*, 035701−035706.
(16) Alabarse, F. G.; Silly, G.; Haidoux, A.; Levelut, C.; Bourgogne, D.; Flank, A.-M.; Lagarde, P.; Pereira, A. S.; Bantignies, J.-L.; Cambon, O.; et al. Effect of H_2O on the Pressure-Induced Amorphization of $AlPO_4$-54·xH_2O. *J. Phys. Chem. C* **2014**, *118*, 3651−3663.
(17) Bordin, R.; Krott, L.; Barbosa, M. High Pressure Induced Phase Transition and Superdiffusion in Anomalous Fluid Confined in Flexible Nanopores. *J. Chem. Phys.* **2014**, *141*, 144502−144508.
(18) Alabarse, F. G.; Rouquette, J.; Coasne, B.; Haidoux, A.; Paulmann, K.; Cambon, O.; Haines, J. Mechanism of H_2O Insertion and Chemical Bond Formation in $AlPO_4$-54·xH_2O at High Pressure. *J. Am. Chem. Soc.* **2015**, *137*, 584−587.
(19) Gavazzoni, C.; Giovambattista, N.; Netz, P. A.; Barbosa, M. C. Structure and Mobility of Water Confined in $AlPO_4$-54 Nanotubes. *J. Chem. Phys.* **2017**, *146*, 234509−234517.
(20) Fabbiani, M.; Polisi, M.; Fraisse, B.; Arletti, R.; Santoro, M.; Alabarse, F.; Haines, J. An In-situ X-ray Diffraction and Infrared Spectroscopic Study of the Dehydration of $AlPO_4$-54. *Solid State Sci.* **2020**, *108*, 106378−106376.
(21) Alabarse, F. G.; Brubach, J.-B.; Roy, P.; Haidoux, A.; Levelut, C.; Bantignies, J.-L.; Cambon, O.; Haines, J. $AlPO_4$-54—$AlPO_4$-8 Structural Phase Transition and Amorphization under High Pressure. *J. Phys. Chem. C* **2015**, *199*, 7771−7779.
(22) de Onate Martinez, J.; McCusker, L. B.; Baerlocher, C. Characterization and structural analysis of differently prepared samples of dehydrated VPI-5. *Microporous Mesoporous Mater.* **2000**, *34*, 99−113.
(23) Clark, R. C.; Reid, J. S. The Analytical Calculation of Absorption in Multifaceted Crystals. *Acta Crystallogr., Sect. A: Found. Crystallogr.* **1995**, *51*, 887−897.
(24) *CrysAlis PRO*, version 171.37.31; Agilent Technologies Ltd: Yarnton, England, 2014.
(25) Dolomanov, O. V.; Bourhis, L. J.; Gildea, R. J.; Howard, J. A.; Puschmann, H. OLEX2: a Complete Structure Solution, Refinement and Analysis Program. *J. Appl. Crystallogr.* **2009**, *42*, 339−341.
(26) Sheldrick, G. M. A Short History of SHELX. *Acta Crystallogr. A* **2008**, *64*, 112−122.
(27) Sheldrick, G. M. Crystal Structure Refinement with SHELXL. *Acta Crystallogr., Sect. C: Struct. Chem.* **2015**, *71*, 3−8.
(28) Fischer, H. E.; Barnes, A. C.; Salmon, P. S. Neutron and X-ray Diffraction Studies of Liquids and Glasses. *Rep. Prog. Phys.* **2006**, *69*, 233−299.
(29) Keen, D. A. A Comparison of Various Commonly used Correlation Functions for Describing total Scattering. *J. Appl. Crystallogr.* **2001**, *34*, 172−177.
(30) Fischer, H. E.; Cuello, G. J.; Palleau, P.; Feltin, D.; Barnes, A. C.; Badyal, Y. S.; Simonson, J. M. D4c: A Very High Precision Diffractometer for Disordered Materials. *Appl. Phys. A* **2002**, *74*, S160−S162.
(31) Ockwig, N. W.; Cygan, R. T.; Hartl, M. A.; Daemen, L. L.; Nenoff, T. M. Incoherent Inelastic Neutron Scattering Studies of Nanoconfined Water in Clinoptilolite and Heulandite Zeolites. *J. Phys. Chem. C* **2008**, *112*, 13629−13634.
(32) Ockwig, N. W.; Greathouse, J. A.; Durkin, J. S.; Cygan, R. T.; Daemen, L. L.; Nenoff, T. M. Nanoconfined Water in Magnesium-Rich 2:1 Phyllosilicates. *J. Am. Chem. Soc.* **2009**, *131*, 8155−8162.
(33) Jiménez-Ruiz, M.; Ferrage, E.; Blanchard, M.; Fernandez-Castanon, J.; Delville, A.; Johnson, M. R.; Michot, L. J. Combination of Inelastic Neutron Scattering Experiments and ab Initio Quantum Calculations for the Study of the Hydration Properties of Oriented Saponites. *J. Phys. Chem. C* **2017**, *121*, 5029−5040.
(34) Jimenez-Ruiz, M.; Ivanov, A.; Fuard, S. LAGRANGE—the new neutron vibrational spectrometer at the ILL. *J. Phys.: Conf. Ser.* **2014**, *549*, No. 012004.
(35) Ivanov, A.; Jimnez-Ruiz, M.; Kulda, J. IN1-LAGRANGE—the New ILL Instrument to Explore Vibration Dynamics of Complex Materials. *J. Phys.: Conf. Ser.* **2014**, *554*, No. 012001.
(36) Roy, P.; Brubach, J.-B.; Calvani, P.; de Marzi, G.; Filabozzi, A.; Gerschel, A.; Giura, P.; Lupi, S.; Marcouillé, O.; Mermet, A.; et al. Infrared Synchrotron Radiation: from the Production to the Spectroscopic and Microscopic Applications. *Nucl. Instrum. Methods Phys. Res., Sect. A* **2001**, *467−468*, 426−436.
(37) Bernardina, S. D.; Alabarse, F.; Kalinko, A.; Roy, P.; Vita, N.; Hienerwadel, R.; Berthomieu, C.; Judeinstein, P.; Zanotti, J.-M.; Bantignies, J.-L.; et al. Experimental Ensembles Used to Study the Dynamics of Water Trapped in Various Media on the AILES Beamline of SOLEIL Synchrotron. *Vib. Spectrosc.* **2014**, *75*, 154−161.
(38) Poulet, G.; Tuel, A.; Sautet, P. A Combined Experimental and Theoretical Evaluation of the Structure of Hydrated Microporous Aluminophosphate AlPO4-18. *J. Phys. Chem. B* **2005**, *109*, 22939−22985.
(39) Perdew, J. P.; Burke, K.; Ernzerhof, M. Generalized Gradient Approximation Made Simple. *Phys. Rev. Lett.* **1996**, *77*, 3865−3868.
(40) Calandrini, V.; Pellegrini, E.; Calligari, P.; Hinsen, K.; Kneller, G. R. nMoldyn-Interfacing Spectroscopic Experiments, Molecular Dynamics Simulations and Models for Time Correlation Functions. *Journ. Neutronique* **2011**, *12*, 201−232.
(41) Kuhs, W. F.; Lehman, M. S. The Structure of the Ice Ih by Neutron Diffraction. *J. Phys. Chem. A* **1983**, *87*, 4312−4313.
(42) Garcia-Pérez, E.; Parra, J. B.; Ania, C. O.; García-Sánchez, A.; van Baten, J. M.; Krishna, R.; Dubbeldam, D.; Calero, S. A Computational Study of CO_2, N_2, and CH_4 Adsorption in Zeolites. *Adsorption* **2007**, *13*, 469−476.
(43) Fois, E.; Gamba, A.; Tilocca, A. Structure and Dynamics of the Flexible Triple Helix of Water inside VPI-5 MolecularSieves. *J. Phys. Chem. B* **2002**, *106*, 4806−4812.
(44) Kolesnikov, A. I.; Anovitz, L. M.; Mamontov, E.; Podlesnyak, A.; Ehlers, G. Strong Anisotropic Dynamics of Ultra-Confined Water. *J. Phys. Chem. B* **2014**, *118*, 13414−13419.
(45) Saitta, A. M.; Datchi, F. Structure and Phase Diagram of High-density Water: The role of Interstitial Molecules. *Phys. Rev. E* **2003**, *67*, No. 020201.
(46) Rahman, A.; Stillinger, F. H. Molecular Dynamics Study of Liquid Water. *J. Chem. Phys.* **1971**, *55*, 3336−3359.
(47) Catafesta, J.; Alabarse, F.; Levelut, C.; Isambert, A.; Hébert, P.; Kohara, S.; Maurin, D.; Bantignies, J.-L.; Cambon, O.; Creff, G.; et al. Confined H_2O Molecules as Local Probes of Pressure-Induced

https://doi.org/10.1021/acs.jpcc.1c01254
J. Phys. Chem. C XXXX, XXX, XXX−XXX

Amorphisation in Faujasite. *Phys. Chem. Chem. Phys.* **2014**, *16*, 12202−12208.
(48) Bove, L. E.; Klotz, S.; Strässle, Th.; Koza, M.; Teixeira, J.; Saitta, A. M. Translational and Rotational Diffusion in Water in the Gigapascal Range. *Phys. Rev. Lett.* **2013**, *111*, No. 18590.
(49) Parker, S. F.; Lennon, D.; Albers, P. W. Vibrational Spectroscopy with Neutrons: A Review of New Directions. *Appl. Spectrosc.* **2011**, *65*, 1325−1341.
(50) Li, J. C. Inelastic Neutron Scattering Studies of Hydrogen Bonding in Ices. *J. Chem. Phys.* **1996**, *105*, 6733−6755.
(51) Li, J.; Kolesnikov, A. I. Neutron Spectroscopy Investigation of Dynamics of Water Ice. *J. Mol. Liq.* **2002**, *100/1*, 1−39.
(52) Crupi, V.; Majolino, D.; Migliardo, P.; Venuti, V. Neutron Scattering Study and Dynamic Properties of Hydrogen-Bonded Liquids in Mesoscopic Confinement. 1. The Water Case. *J. Phys. Chem. B* **2002**, *106*, 10884−10894.
(53) Ramasay, J. D. F.; Lauter, H. J. Tompkinson, Inelastic Neutron Scattering of Water and Ice in Porous Solids. *J. Phys. Colloques* **1984**, *45*, C7-73−C7-79.
(54) Brubach, J.-B.; Mermet, A.; Filabozzi, A.; Gerschel, A.; Roy, P. Signatures of the Hydrogen Bonding in the Infrared Bands of Water. *J. Chem. Phys.* **2005**, *122*, 184509−184516.
(55) Alabarse, F. G.; Silly, G.; Brubach, J.-B.; Roy, P.; Haidoux, A.; Levelut, C.; Bantignies, J.-L.; Kohara, S.; Le Floch, S.; Cambon, O.; et al. Anomalous Compressibility and Amorphization in $AlPO_4$-17, the Oxide with the Highest Negative Thermal Expansion. *J. Phys. Chem. C* **2017**, *121*, 6852−6863.
(56) Arakawa, M.; Kagi, H.; Fukazawa, H. Laboratory Measurements of Infrared Absorption Spectra of Hydrogen-Ordered Ice: A Step to the Exploration of Ice XI in Space. *Astrophys. J., Suppl. Ser.* **2009**, *184*, 361−365.
(57) Geiger, P.; Dellago, C.; Macher, M.; Franchini, C.; Kresse, G.; Bernard, J.; Stern, J. N.; Loerting, T. Proton Ordering of Cubic Ice Ic: Spectroscopy and Computer Simulations. *J. Phys. Chem. C* **2014**, *118*, 10989−10997.
(58) Zanotti, J.-M.; Judeinstein, P.; Dalla-Bernardina, S.; Creff, G.; Brubach, J.-B.; Roy, P.; Bonetti, M.; Ollivier, J.; Sakellariou, D.; Bellissent-Funel, M.-C. Competing Coexisting Phases in 2D Water. *Sci. Rep.* **2016**, *6*, No. 25938.
(59) Chen, S.-H.; Liu, L.; Faraone, A. Chen, Liu, and Faraone reply. *Phys. Rev. Lett.* **2006**, *97*, No. 189803.
(60) Alcoutlabi, M.; McKenna, G. B. Effects of Confinement on Material Behaviour at the Nanometre Size Scale. *J. Phys.: Condens. Matter* **2005**, *17*, R461−R524.
(61) Findenegg, G. H.; Jahnert, S.; Akcakayiran, D.; Schreiber, A. Freezing and Melting of Water Confined in Silica Nanopores. *Chem. Phys. Chem.* **2008**, *9*, 2651−2659.

https://doi.org/10.1021/acs.jpcc.1c01254
J. Phys. Chem. C XXXX, XXX, XXX−XXX